ELSEVIER

Clinical Neurophysiology 111 (2000) 81–92

www.elsevier.com/locate/clinph

Technical report

High-resolution EEG mappings: a spherical harmonic spectra theory and simulation results

Yao Dezhong*

Department of Automation, University of Electronic Science and Technology of China, Chengdu 610054, People's Republic of China

Accepted 2 August 1999

Abstract

Shown first is the equivalence between the multiple expansion (ME) of the brain electrical generator and the spherical harmonic spectra (SHS) of the potential generated by the electrical generator in an infinite volume conductor. Based on the equivalence, the SHS and the spatial filters which connect the SHS with the ME are deduced, in a concentric 3 sphere conductor and for the 5 EEG source mappings. They are cortical potential mapping (CPM), scalp Laplacian mapping (LM), pseudo-cortical potential mapping (PCPM), equivalent dipole layer mapping (EDM) and equivalent charge layer mapping (ECM). The theoretical simulation study of the spatial filters and mappings indicate that all 5 mappings provide higher resolution imaging maps of brain electrical activity than the scalp potential map. In the inverse problem, a spherical spline fit algorithm is provided to reconstruct the SHS of the scalp recording potential, and then the SHS and maps of the 5 mappings are reconstructed by utilizing the spatial filters and the SHS of the scalp potential. The results indicate that the correlativity order between a reconstructed map and the actual cortical potential map is CPM $\geq$ EDM $>$ PCPM $>$ LM $>$ ECM. An empirical VEP data study shows that any one of the 5 mappings also provides higher spatial resolution than the scalp potential map.

Keywords: High-resolution EEG mapping; Cortical imaging; Multiple expansion; Spherical harmonic spectra; Visual evoked potential

1. Introduction

Conventional scalp EEG mapping suffers from limited spatial resolution because of the spatial smearing and other distortions existing in the head volume conductor (Nunez et al., 1994). A few approaches have been developed to construct an invasive high-resolution mapping, which have been increasingly used in recent years (Ahlfors et al., 1992; Manahilov et al., 1992; Sidman et al., 1992; Towle et al., 1995; Gevins, 1998).

1.1. Scalp Laplacian mapping (LM)

LM estimate is based on the 2D Laplace operation on the scalp potential. LM is related to the current source density (Hjorth, 1975). There are many versions of the Laplacian estimate (Nunez et al., 1994), ranging from the use of groups of 5 or more local electrodes (Hjorth, 1975; Nunez, 1981; Gevins, 1989) to global measures based on spline fits to recorded potentials (Pascual-Marqui et al., 1988; Perrin et al., 1989; Nunez, 1989; Le et al., 1992; Law and Nunez, 1993; Babiloni et al., 1996; Zhao et al., 1998), and from a spatial filtering of EEG (Srinivasan et al., 1996) to a numeric algorithm for a realistic head model (Oostendorp and Oosterom, 1996).

1.2. Equivalent dipole layer mapping (EDM)

EDM estimate is based on the spatial deconvolution technique. A few different models of the volume conductor as well as different source models have been used. A primary report was the 'software lens' which was based on a half-space volume conductor model, and the 'spatial deconvolution technique' was involved to deconvolve the scalp potential to get a small local dipole distribution (Freeman, 1980; Nunez, 1987). The later works include local-plane models (Hamalainen and Ilmoniemi, 1984; Wang et al., 1992; Baillet and Garnero, 1997), a realistic cortical surface model (Srebro, 1996; Srebro and Oguz, 1997) and a closed spherical surface model (He and Yao et al., in preparation). In general, since the location of the actual source is unknown, each of the above estimated dipole distributions is an equivalent distribution source in generating the same scalp potential, so it is a mapping of the actual brain electrical generator.

* *E-mail address:* dyao@uestc.edu.cn.

1388-2457/00/$ - see front matter CLINPH 99544
PII: S1388-2457(99)00205-9

1.3. Cortical potential mapping (CPM)

CPM estimates have been obtained by various approaches. One approach is to construct a spherical equivalent dipole layer between the actual sources and the cortical surface by the spatial deconvolution technique, and then the cortical surface potential is reconstructed from the obtained dipole layer. This approach is termed as cortical imaging technique (CIT, Sidman et al., 1990). Various versions cover a hemisphere radial dipole layer in a single sphere head model (Sidman et al., 1990; Sidman et al., 1992; Kearfott et al., 1991; Yao, 1995a; 1996a), a closed radial dipole layer in a concentric 3 sphere model (Kearfott et al., 1991; He et al., 1996; Wang and He, 1998) and a closed dipole layer in a 3 layer head volume conductor with realistic shape (Babiloni et al., 1997; Zanow, 1997). The second approach is to construct a spherical equivalent charge layer by the same mathematical algorithm, and in order to distinguish the two approaches, the first approach has been re-termed as dipole-CIT (DCIT), and the second one charge-CIT (CCIT) (Yao, 1995a, 1996a). It has been found that the analytical solution of the strength of the equivalent dipole layer is proportional to the electrical potential over the same spherical surface when the exterior space of the dipole layer is replaced by air (Fig. 1c), and the strength of the equivalent charge layer is the current density while the exterior space of the layer is replaced by a perfect conductor (Fig. 1d) (Yao, 1995b; Yao and Luo, 1996a, Yao et al., in preparation). The equivalent dipole layer has been tested as a high-resolution mapping (He and Yao, in preparation), and the equivalent charge layer will be tested as a new high-resolution imaging map in this paper, i.e. the equivalent charge layer mapping (ECM). The third approach to reconstruct the cortical potential is the direct numeric algorithm, which may be a boundary element method (BEM) (Srebro et al., 1993; He et al., 1997; Van Burik et al., 1997), or a finite element method (FEM) (Gevins et al., 1993; Le and Gevins, 1993; Gevins, 1998). The fourth approach is the spherical harmonic analysis algorithm, which has been implemented on a single homogeneous sphere head model (Yao, 1995c, 1996b; Yao and Luo, 1996b), and on a concentric multi-sphere model (Srinivasan et al., 1996; Edlinger et al., 1998). The theoretical basis is the multiple expansion (ME) of the brain electrical generator, so it is also an equivalent source technique (Yao, 1996b).

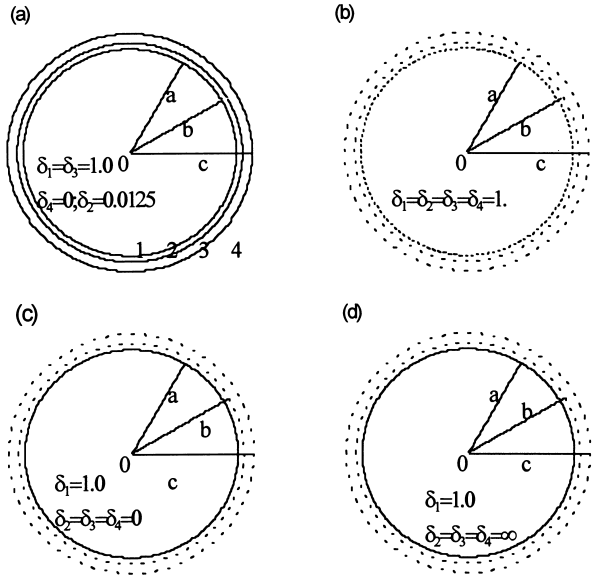

Fig. 1. Conductor model. (a) Concentric 3 sphere conductor head model. (b) Equivalent conductor model corresponding to the pseudo-cortical potential calculation. (c) Equivalent conductor model corresponding to the equivalent dipole layer at $r = 0.87$. (d) Equivalent conductor model corresponding to the equivalent charge layer at $r = 0.87$. Where *a, b* and *c* are the radii of the three spheres, δi is the regional conductivity, $i = 1, 2, 3, 4$.

1.4. Pseudo-cortical potential mapping (PCPM)

PCPM is defined as the cortical potential generated by the brain electrical generator when the whole exterior space of the cortical layer is filled with a volume conductor of the same conductivity as the inner brain (Fig. 1b). One approach has been reported to implement the PCPM by DCIT. After getting the dipole layer through DCIT, the PCPM is reconstructed by the potential generated by the equivalent dipole layer in an infinite homogeneous conductor (Yao and Qi, 1995).

In this paper, we do not focus on any particular algorithm, because many numeric details and promising results about the various mappings have been reported, and even better results may be provided with the development of computation technique and resource in the future. What we are interested here are the relations among the 5 mappings and their relative performances under a unified implementation frame. In this paper, the spatial spectra filters connecting the SHS of the five mappings with the ME of the brain electrical generator are deduced in Section 2. In Section 3, a sphere spline fit algorithm is introduced to get the inverse SHS of the scalp potential, and then the five maps are deduced from the obtained SHS and the respective spatial filters. A comparison of the mappings is completed by tests on theoretical simulation data and empirical data in Sections 2 and 3. A summary and discussion is given in Section 4.

2. Forward theory

2.1. The ME of a dipole and SHS of potential in an infinite conductor

Fig. 1b is regarded as the physical model of an infinite conductor, and the potential distribution of an arbitrarily positioned and orientated dipole in an infinite medium is given through the following sets of formulae (Stratton, 1941):

$$\Phi_\infty = \frac{1}{4\pi\delta_1}\vec{P}\cdot\nabla_{r_0}\left(\frac{1}{r_p}\right)$$

$$= \frac{1}{4\pi\delta_1}\left\{P_r\frac{\partial}{\partial r_0} + P_\varphi\frac{1}{r_0\sin\theta_0}\frac{\partial}{\partial\varphi_0} + P_\theta\frac{1}{r_0}\frac{\partial}{\partial\theta_0}\right\}\frac{1}{r_p}$$

$$= \sum_{l=1}^{\infty}\sum_{m=0}^{l}\frac{1}{r^{l+1}}(g_l^m\cos m\varphi + h_l^m\sin m\varphi)P_l^m(\cos\theta)$$

$$= \sum_{l,m}\frac{1}{r^{l+1}}S_l^m(\vec{P},\theta,\varphi), r > r_0 \quad (1)$$

Where

$$S_l^m(\vec{P},\theta,\varphi) = (g_l^m\cos m\varphi + h_l^m\sin m\varphi)P_l^m(\cos\theta) \quad (2)$$

And

$$g_l^m = \frac{r_0^{l-1}}{4\pi\delta_1}(2-\delta_{m0})\frac{(l-m)!}{(l+m)!}(lP_rP_l^m(\cos\theta_0)\cos m\varphi_0 - \frac{mP_\varphi}{\sin\theta_0}P_l^m(\cos\theta_0)\sin m\varphi_0 - \frac{P_\theta}{2}((l-m+1)(l+m)P_l^{m-1}(\cos\theta_0) - P_l^{m+1}(\cos\theta_0))\cos m\varphi_0)h_l^m$$

$$= \frac{r_0^{l-1}}{4\pi\delta_1}(2-\delta_{m0})\frac{(l-m)!}{(l+m)!}(lP_rP_l^m(\cos\theta_0)\sin m\varphi_0 + \frac{mP_\varphi}{\sin\theta_0}P_l^m(\cos\theta_0)\cos m\varphi_0 - \frac{P_\theta}{2}((l-m+1)(l+m)P_l^{m-1}(\cos\theta_0) - P_l^{m+1}(\cos\theta_0))\sin m\varphi_0) \quad (3)$$

Where (r_0,θ_0,ϕ_0) and (r,θ,ϕ) are the spherical coordinates of the location of a dipole source and its field point, r_p is the distance between the source location and the field point, P_l^m is the associated Legendre function of degree l and order m. δ_1 is the conductivity of the conductor model. δ_{m0} is the Kronecker delta. The (P_r,P_θ,P_ϕ) is the dipole moment in the spherical coordinate system. Practically, the degree l is terminated at $L_{\max}$. Based on Eq. (1), on one hand, in an infinite volume conductor the potential, generated by a dipole, can be represented by an orthogonal spherical harmonic series, where the coefficients g_l^m, h_l^m are the spherical harmonic spectra (SHS) of the potential. On the other hand, each spherical harmonic function is related to a multiple source at the origin, that is to say, the actual dipole is equivalent to a multiple series, while the multiple series is the multiple expansion (ME) at the origin of the brain electrical generator. The ME of the actual sources is determined uniquely by the source model and the coordinate system. And in the infinite volume conductor, the strength of the multiple is directly related to the value of the SHS component of the potential.

Fig. 2 shows a few normalized maps of the basis function of the spherical harmonic analysis. From the maps, it is clear that the number of peaks is the same as the order m, and the larger the degree l is, the sharper the peak is.

2.2. The SHS of the potentials in a concentric 3 sphere model

Among the various head models, the concentric 3 sphere model is the most popular one, especially in simulation study. In fact, the head has been successfully regarded as a series of concentric regions (the aforementioned brain, skull and scalp), as illustrated in Fig. 1a (Rush and Driscoll, 1968; 1969). In this model, the inner and outer radii of the skull are chosen to be 8 and 8.5 cm, respectively, while the radius of the head is 9.2 cm. For the brain and the scalp, the resistivity is 2.22 Ω, whereas the skull's resistivity is $80\times 2.22\ \Omega = 177\ \Omega$.These numerical values are given solely to indicate typical (mean) physiological quantities. In theoretical simulation study, these numerical values may be normalized to their relative values. The radii are normalized by the radius of the head, and the final results are a = 0.87, b = 0.92 and c = 1.0. The resistivity is normalized by the skull's resistivity, and the finial conductivity is $\delta_1 = \delta_3 = 1.0$, $\delta_2 = 0.0125$.

The electrostatic boundary condition of the concentric 3 sphere conductor requires that the potential and normal current are continuous across the boundaries, and then we get the SHS of the potential in each sub-region:

$$\Phi(i) = \sum_{l,m}\frac{K_l(i)}{r^{l+1}}S_l^m = \sum_{l,m}\frac{1}{r^{l+1}}(G_l^m(i)\cos m\varphi + H_l^m(i)\sin m\varphi)P_l^m(\cos\theta) \quad (4)$$

$$G_l^m(i) = K_l(i)g_l^m, H_l^m(i) = K_l(i)h_l^m \quad (5)$$

$$a \geq r > r_0, i = 1; b \geq r \geq a, i = 2; c \geq r \geq b, i = 3$$

Where, $i = 1, 2, 3$, respectively, represents the inner-sphere region-brain region, the skull and the scalp region (Fig. 1a), and

$$K_l(1) = A_l r^{2l+1} + 1$$

$$K_l(2) = B_l(r^{2l+1} + \gamma)$$

$$K_l(3) = E_l(r^{2l+1} + \chi) \quad (6)$$

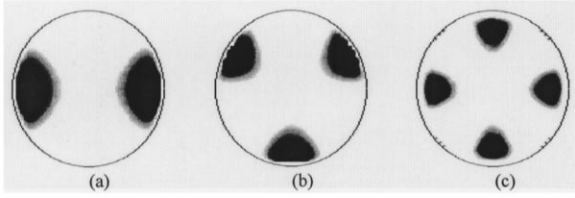

Fig. 2. Normalized maps of a few basis functions of the spherical harmonic spectra. Where the black is corresponding to the maximum, and the white is corresponding to the minimum. These basis functions are: (a) $P_3^2\cos 2\varphi$; (b) $P_4^3\sin 3\varphi$; (c) $P_6^4\cos 4\varphi$.

$$A_l = \frac{(2l+1)(1+\gamma a^{-(2l+1)})}{l(1-s)a^{2l+1} + \gamma(l+s(l+1))} - a^{-(2l+1)} \tag{7}$$

$$B_l = \frac{2l+1}{l(1-s)a^{2l+1} + \gamma(l+s(l+1))} \tag{8}$$

$$E_l = B_l(b^{2l+1} + \gamma)\frac{l+1}{(l+1)b^{2l+1} + lc^{2l+1}} \tag{9}$$

$$s = \frac{\delta_2}{\delta_1} = \frac{\delta_2}{\delta_3}, f = b/c, \chi = \frac{l}{l+1}c^{2l+1} \tag{10}$$

$$\alpha = f^{2l+1}(1-s) - (1 + \frac{ls}{1+l})$$

$$\beta = f^{-(2l+1)}(1-s) - (1 + \frac{l+1}{l}s), \gamma = \alpha/\beta \tag{11}$$

Where G_l^m and H_l^m are the SHS of the potential Φ in the concentric 3 sphere conductor model. Especially, when $r = a$, $\Phi(1) =$ cortical surface potential, and when $r = c$, $\Phi(3) =$ scalp surface potential.

$K_l(i)$ $(i = 1,2,3)$ are the spatial spectra filters that connect the SHS of the potential in a sub-region with the ME of the brain electrical generator. In the homogenized infinite conductor model shown by Fig. 1b and Eq. (1), the spatial filter may be termed as $K_l(0) = 1.0$, which is an all-pass spatial filter. As the $K_l(i)$ $(i = 1,2,3)$ are determined by the volume conductor model, the SHS of the potential in the concentric 3 sphere conductor depends not only on the source model, the ME, but also on the conductor model, the spatial filter. And the PCPM may be explained as the result that the conductor filter effect is removed or compensated by an inverse filter. The numeric results of the spatial filters shown by Fig. 3a,e demonstrate the low-pass or smearing characteristics of the concentric 3 sphere conductor.

2.3. The SHS of LM, EDM and ECM

Among the five mappings, the SHS of the PCPM is given by g_l^m, h_l^m and the SHS of the CPM is given by $G_l^m(1)$, $H_l^m(1)$ within $r \le a$. Now we consider the SHS of the other three mappings.

2.3.1. The SHS of the ECM

The ECM is the strength map of the equivalent charge layer that generates the same potential outside the layer as the actual source does. For a spherical equivalent layer, the analytic solution of the equivalent charge strength has been derived by expecting the potential equivalence (Yao, 1995b; Yao and Luo, 1996a):

$$S_q = \delta_1 \sum_{l,m} \frac{2l+1}{r^{l+2}} S_l^m(\vec{P}, \theta, \varphi)$$

$$= \sum_{l,m}^{\infty} \frac{1}{r^{l+1}}\left(G_l^m(q)\cos m\varphi + H_l^m(q)\sin m\varphi\right)p_l^m(\cos\theta), r \le a \tag{12}$$

Where the SHS of the ECM are

$$G_l^m(q) = K_l(q)g_l^m, H_l^m(q) = K_l(q)h_l^m \tag{13}$$

And the spatial filter is

$$K_l(q) = \delta_1(2l+1)/r, r \le a \tag{14}$$

Apparently, the key factor is $(2l + 1)$, which is a high spatial frequency amplifying factor as illustrated in Fig. 3f.

2.3.2. The SHS of the EDM

The EDM is the strength map of the equivalent dipole layer in DCIT. For a spherical closed layer, the analytic solution is (Yao, 1995b; Yao and Luo, 1996a):

$$S_d = \delta_1 \sum_{l=0}^{\infty}\sum_{m=0}^{l} \frac{2l+1}{l}\frac{1}{r^{l+1}} S_l^m(\vec{P}, \theta, \varphi)$$

$$= \sum_{l=0}^{\infty}\sum_{m=0}^{l} \frac{1}{r^{l+1}}\left(G_l^m(d)\cos m\varphi + H_l^m(d)\sin m\varphi\right)p_l^m(\cos\theta), r \le a \tag{15}$$

Where the SHS of the EDM are

$$G_l^m(d) = K_l(d)g_l^m, H_l^m(d) = K_l(d)h_l^m \tag{16}$$

And the spatial filter is

$$K_l(d) = \delta_1(2l+1)/l = 2 + 1/l \tag{17}$$

As S_d is proportional to the scalp potential of a homogeneous volume conductor head model (Yao et al., in preparation), $K_l(d) \sim 1/l$ also means that the head-air boundary functions as a low-pass filter as illustrated in Fig. 3g.

2.3.3. The SHS of the LM

The scalp Laplacian is defined by

$$L_{\text{scalp}} = -\frac{1}{r^2}\frac{\partial}{\partial r}\left(r^2\frac{\partial \Phi(3)}{\partial r}\right)\Big|_{r=c}$$

$$= -\sum_{l,m}\left[E_l l(l+1)r^l + (l+1)l\chi E_l \frac{1}{r^{l+1}}\right]_{r=c}\frac{1}{c^2}S_l^m$$

$$= \sum_{l,m}\frac{K_l(L)}{c^{l+1}}S_l^m = \sum_{l,m}\frac{1}{c^{l+1}}(G_l^m(L)\cos m\varphi + H_l^m(L)\sin m\varphi)P_l^m(\cos\theta) \tag{18}$$

Where the SHS of the LM are

$$G_l^m(L) = K_l(L)g_l^m, H_l^m(L) = K_l(L)h_l^m \tag{19}$$

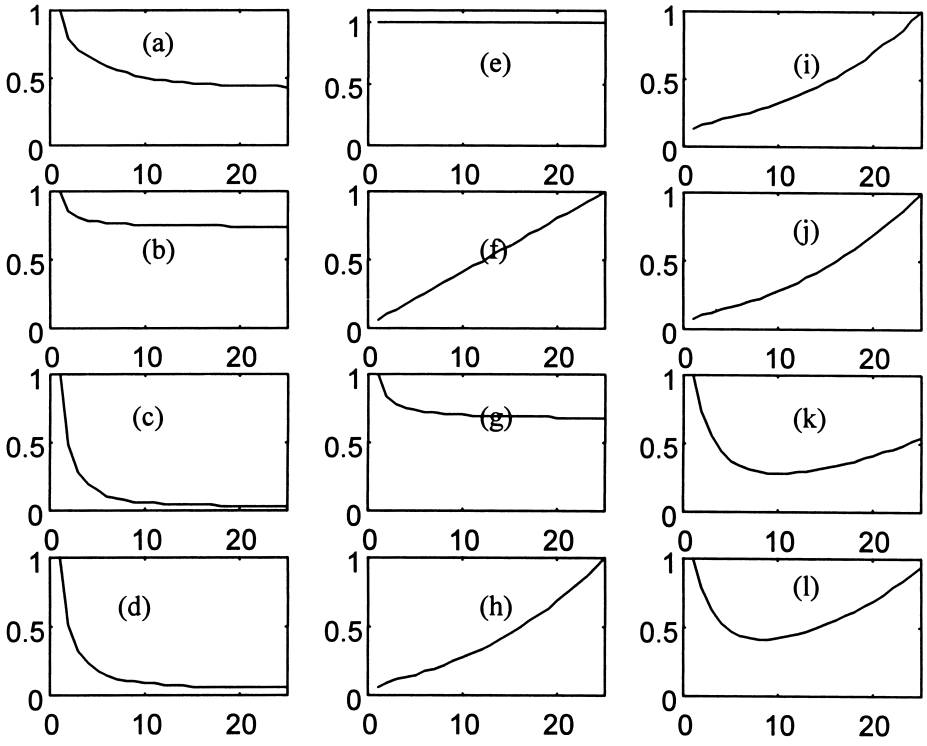

Fig. 3. Normalized amplitude versus degree l of the spatial filter K_l. The horizontal axis is the degree l, and the vertical axis is the normalized amplitude. (a) and (b) show $K_l(1)$, respectively, at $r = 0.80, 0.87$, (c) shows $K_l(2)$ at $r = 0.92$ and (d) shows $K_l(3)$ at $r = 1.0$, they correspond to the 3 sphere conductor model; (e) shows $K_l(0)$ at $r = 1.0$, it corresponds to the infinite conductor model; (f) shows $K_l(q)$, it corresponds to the equivalent charge layer model; (g) shows $K_l(d)$, it corresponds to the equivalent dipole layer model; (h) shows$K_l(L, 0) = l(l + 1)$, it corresponds to the Laplacian operator; (i,l) shows $K_l(L, i) = K_l(i)K_l(L, 0)$ $i = 1, 2, 3$ at $r = 0.80$ ($i = 1$), 0.87 ($i = 1$), 0.92 ($i = 2$) and 1.0 ($i = 3$), respectively.

And the spatial filter is

$$K_l(L) = -(E_l(c^{2l+1} + \chi))(l + 1)l/c^2 = -K_l(3)(l + 1)l/c^2 \quad (20)$$

It is easy to get the Laplacian in other regions, and the spatial filter is:

$$K_l(L, i) = -K_l(i)(l + 1)l/r^2 \quad (21)$$

Where $a \geq r > r_0$, $i = 1$; $b \geq r \geq a$, $i = 2$;$c \geq r \geq b$, $i = 3$. As a mapping technique, the negative sign is omitted in the following discussion, and the filters are re-noted as $K_l(L, 0) = l(l + 1)$ and $K_l(L, i) = K_l(L, 0)K_l(i), i = 1, 2, 3$. Their spectra characteristics are shown by Fig. 3h–l.

2.4. Forward simulation and discussion

2.4.1. The spatial filters

The above analyses show that the spatial filter K_l plays the role of connecting the ME of the EEG electrical generator with the SHS of the various quantities. Fig. 3 shows the normalized amplitude versus the degree l of the spatial filter K_l. From the curves, in the concentric 3 sphere conductor, the relative value (the ratio of the amplitude of the spatial filter at degree $l = 10$ and that at degree $l = 1$) is 0.0879 (Fig. 3d) on the scalp surface at $r = 1.0$, 0.7532 (Fig. 3b) on the cortical surface at $r = 0.87$, 0.5040 (Fig. 3a) on the layer at $r = 0.80$, and for LM, EDM and ECM, the relative values are 4.836 (Fig. 3h), 0.70 (Fig. 3g) and 7.0 (Fig. 3f) respectively. Comparing with the filter $K_l(0)$ of the PCPM (Fig. 3e), it is clear that the LM and ECM will result in ‘ higher’ resolution mappings, and the CPM and EDM will result in ‘ lower’ resolution mappings. The EDM (Fig. 3g) will result in a similar resolution map to what the CPM does at $r = 0.87$ (Fig. 3b). The $K_l(L,3)$ of the LM (scalp Laplacian) reaches at a minimum relative value 0.4174 at degree $l = 8$ and a relative value 0.4252 at degree $l = 10$ (Fig. 3l). The LM values 0.4252 at $l = 10$ and $r = 1.0$ is smaller than the CPM values 0.7532 at $l = 10$ and $r = 0.87$ (Fig. 3l vs. Fig. 3b), combining with the fact that the resolvable degree from a noisy scalp recording is also around $l = 10$ (Edlinger et al., 1998), which may serve as a reason of the conclusion that the CPM at $r = 0.87$ is better than LM at $r = 1.0$ obtained in a theoretical simulation study (Nunez et al., 1994).

2.4.2. The forward maps

Let’s suppose there are three dipoles in the concentric 3 sphere conductor, the first two unit radial dipoles locating at the Cartesian coordinates (− 0.6, − 0.3, 0.3) and (− 0.6, 0.3, 0.3), with their radial spherical coordinates being as $r_0 = 0.7348$; the third radial dipole locating at (0.0, 0.2, 0.7), its radial spherical coordinate being as $r_0 = 0.7280$, and its moment as 0.5.

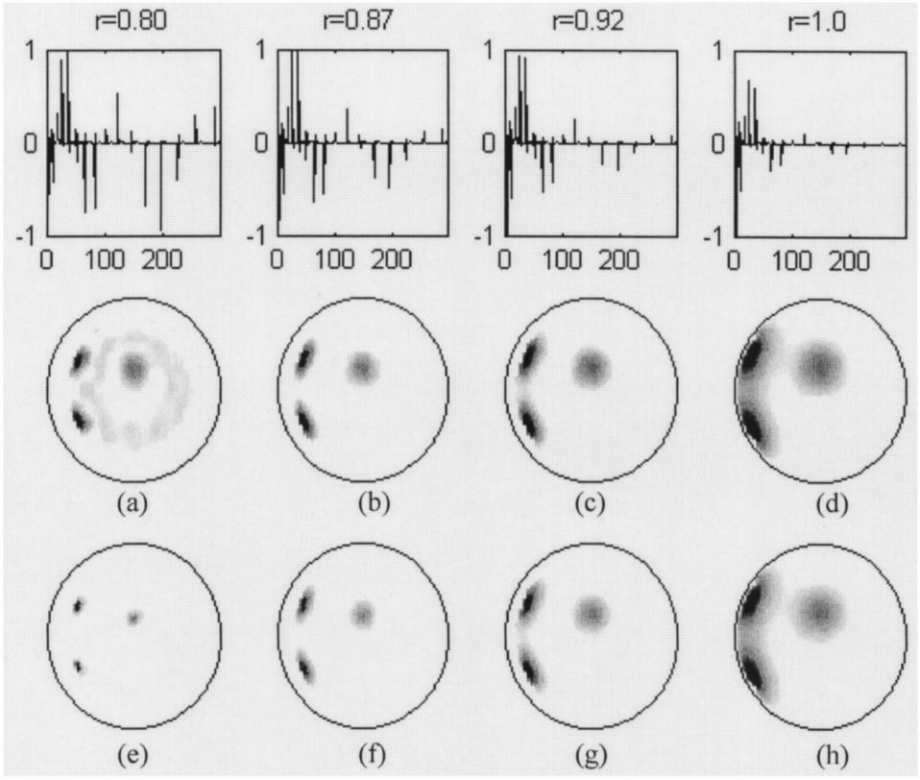

Fig. 4. The normalized SHS and maps of the three dipoles in the infinite conductor. The first row shows the normalized SHS, respectively, at $r = 0.80$, 0.87, 0.92 and 1.0, where the horizontal axis is the order number of the SHS. Its range is from $l = 1$, g_1^0, g_1^1, h_1^1 to $l = Lmax$, $g_{Lmax}^0, ..., g_{Lmax}^{Lmax}, h_{Lmax}^{Lmax}$, and the total number is $Lmax*Lmax + 2Lmax$, here the first 300 points are plotted. The second row shows the maps constructed by setting $Lmax = 15$ (the total number of the SHS component is 255), and the third row shows the maps constructed by setting $Lmax = 150$ (the total number is 22 800) at $r = 0.80$, 0.87, 0.92 and 1.0, respectively.

Fig. 4 shows the normalized SHS and maps of the potentials of the three dipoles in the infinite conductor. Fig. 5 shows the normalized SHS and maps of the potentials of the same source configuration in the concentric 3 sphere conductor and Fig. 6 shows the normalized SHS and maps of the derived imaging maps LM, EDM and ECM. The second rows of Figs. 4–6 are constructed by setting $L_{max} = 15$, and the third rows are constructed by setting $L_{max} = 150$. It is difficult to distinguish the three sources from the map of the scalp recording potential (Fig. 5d,h at $r = 1.0$), however, they are clearly distinguished by the PCPM at $r = 0.80$, 0.87, 0.92 and 1.0 (Fig. 4a,h). And the differences between Figs. 4 and 5 are due to the smearing effect of the concentric 3 sphere conductor (Fig. 3a,d vs. Fig. 3e). Based on Fig. 6, the three sources are distinguished by the EDM (Fig. 6c,h) at $r = 0.80$, Fig. 6d,i at $r = 0.87$), the ECM (Fig. 6a,f at $r = 0.80$, Fig. 6b,g at $r = 0.87$), LM (Fig. 6e,j), and the CPM (Fig. 5a,e at $r = 0.80$, Fig. 5b,f at $r = 0.87$). In these maps, it is clear that the deeper the imaging depth is and the higher the degree number l is, the higher the spatial resolution of the imaging map is, which are illustrated by the maps at $r = 0.80$ versus the maps at $r = 0.87$, and the second row of Figs. 4–6 versus the third row of Figs. 4–6. These forward maps show the possibility of their being used as high-resolution mappings of the brain electrical generator.

3. Inverse problem

According to the forward theory derived in the last section, only in the infinite volume conductor, the strength of a multiple is directly related to the value of a SHS component of the potential. However, it is connected with the ME by the spatial filters that the SHS of the potentials in the concentric 3 sphere conductor model and of the five imaging maps. And it is the spatial filters that provide relations among the SHS of the five high-resolution mappings and the ME of the brain electrical generator. In the EEG inverse problem, the known is the non-invasive scalp recording potential. If we get the SHS of the scalp recording potential by an inverse algorithm, we obtain the ME of the brain electrical generator by applying an inverse filter to compensate the spatial filter $K_l(3)$. Since the ME provides the complete information of the generator, the five high-resolution mappings are easily derived from the ME by attaching the respective spatial filter to the ME. Here, a sphere spline fit algorithm is introduced to get the SHS of the scalp poten-

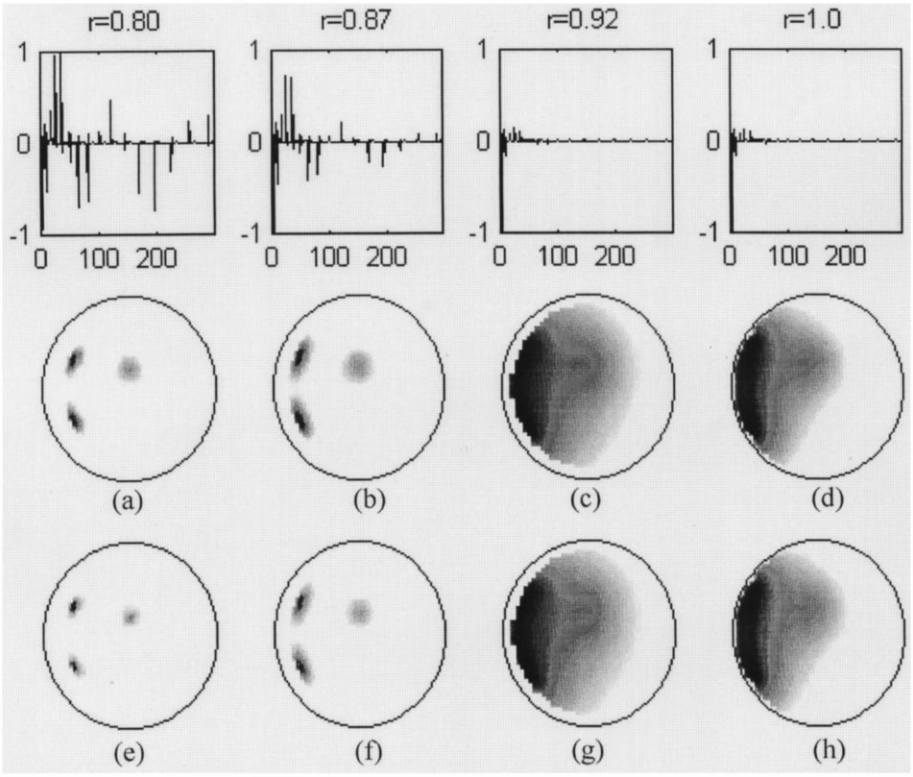

Fig. 5. The normalized SHS and maps of the three dipoles in the concentric 3 sphere conductor. The first row shows the normalized SHS at $r = 0.80, 0.87, 0.92$ and 1.0. where the horizontal axis is the order number of the SHS. Its range is from $l = 1$, $G_1^0(i)$, $G_1^1(i)$, $H_1^1(i)$, to $l = Lmax$, $G_{Lmax}^0(i)$, ..., $G_{Lmax}^{Lmax}(i)$ $H_{Lmax}^{Lmax}(i)$ ($i = 1$ at $r = 0.80$ and 0.87, $i = 2$ at $r = 0.92$ and $i = 3$ at $r = 1.0$), here the first 300 points are plotted. The second row shows the maps constructed by setting $Lmax = 15$ and the third row shows the maps constructed by setting $Lmax = 150$ at $r = 0.80$, 0.87, 0.92 and 1.0, respectively.

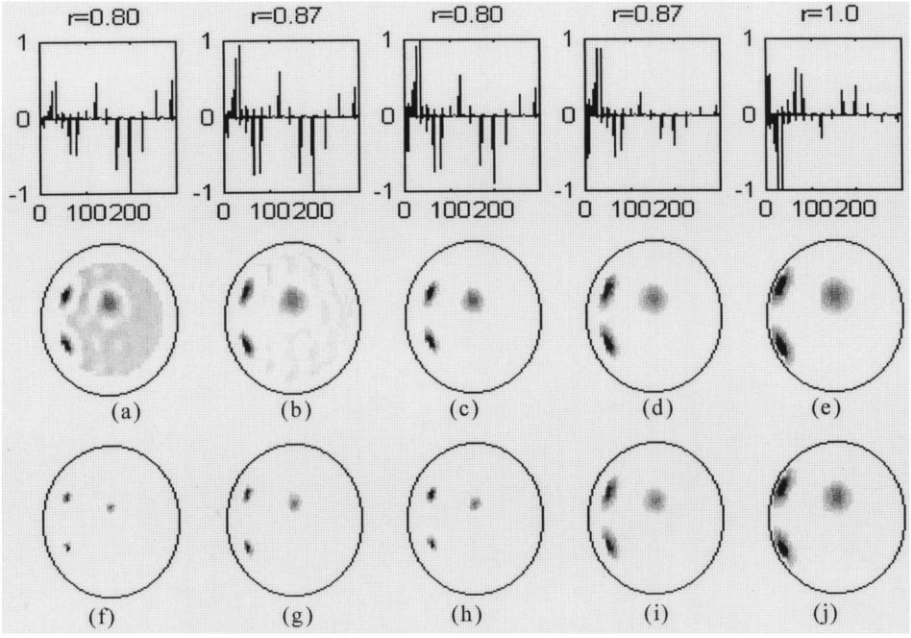

Fig. 6. The normalized SHS and maps of the LM, ECM and EDM of the three dipoles in the concentric 3 sphere conductor. The first row shows the normalized SHS. The horizontal axis is the order number of the SHS, and its range is from $l = 1$, $G_1^0(i)$, $G_1^1(i)$, $H_1^1(i)$, to $l = Lmax$, $G_{Lmax}^0(i)$, ..., $G_{Lmax}^{Lmax}(i)$, $H_{Lmax}^{Lmax}(i)$, here the first 300 points are plotted. From left to right, they are, respectively, the SHS of the ECM at $r = 0.80$ and 0.87 where $i = q$, of the EDM at $r = 0.80$ and 0.87 where $i = d$, and of the LM at scalp surface at $r = 1.0$. The second and third rows show the corresponding maps, where the second row is the maps constructed by setting $Lmax = 15$ and the third row is the maps constructed by setting $Lmax = 150$.

tial: $G_l^m(3)$, $H_l^m(3)$ and the others are obtained by using the respective spatial filter.

3.1. Sphere spline fit and inverse algorithm

The sphere spline function (Wahba 1981) has been used in EEG mapping research (Perrin et al., 1987; , 1989; Pascual-Marqui et al., 1988; Biggins et al., 1991; Edlinger et al., 1998). Defining

$$W(u,v)=\sum_{l=1}^{Lmax}\sum_{m=0}^{l}\frac{1}{4\pi}\frac{2l+1}{(l(l+1))^n}(2-\delta_{m0})$$

$$\times\{\tilde{p}_l^m(\cos\theta_u)\cos m\varphi_u\tilde{p}_l^m(\cos\theta_v)\cos m\varphi_v$$

$$+\tilde{p}_l^m(\cos\theta_u)\sin m\varphi_u\tilde{p}_l^m(\cos\theta_v)\sin m\varphi_v\}$$

$$=\sum_{l=1}^{Lmax}\frac{1}{4\pi}\frac{2l+1}{(l(l+1))^n}P_l(\cos\gamma_{uv})$$

$$\tilde{p}_l^m(\cos\theta)=\sqrt{\frac{(l-m)!}{(l+m)!}}p_l^m(\cos\theta) \tag{22}$$

The spline interpolation formula is

$$\Phi(R_{scalp},\theta_u,\varphi_u)=\sum_{v=1}^{Ne}W(u,v)X(v)+d \tag{23}$$

Where n is chosen to be 2 in Edlinger et al. (1998) and 4 in Perrin et al. (1989). Here it is chosen to be 2. $\tilde{p}_l^m(\cos\theta)$ is the associated normalized Legendre function. The

γ_{uv}

is the angle between electrode location u and location v, and X is an unknown column vector of the spherical spline coefficients and d is an unknown constant. The $X(v)s$ are the solutions of (Perrin et al., 1989)

$$\Phi=WX+Td$$

$$T'X=0 \tag{24}$$

Where T is a column vector with each of its element being unity. Here we replace the problem (24) with the following equivalent problem

$$\min|(\Phi-WX_1)-T<\Phi-WX_1>|$$

$$\Rightarrow|(\text{Noise}+Td)-T<\text{Noise}+Td>|=|\text{Noise}| \tag{25}$$

Where it is supposed that the expectation $\langle Noise\rangle$ is zero, and the covariance of the noise is known. The vector X_1 in Eq. (25) is estimated by using the general inverse and the discrepancy-principle regularization (Kirsch, 1996). For application, the covariance of the noise may be estimated approximately. The constraint on the sum of X in Eq. (24) is satisfied by defining

$$X=X_1-T<X_1> \tag{26}$$

In theory, $d=0$ and it is not included in Eq. (4). Practically, since the number of observation points is finite, d will not be zero. However, in our algorithm, d is excluded by the discrepancy-principle regularization implicitly (Eq. (25)). Besides, $Lmax=15$ is chosen in the inverse calculation.

After we get X through Eqs. (24)–(26), by involving Eq. (22) into Eq. (23), and comparing the final Eq. (23) with Eq. (4), we get the SHS of the scalp potential

$$G_l^m(3)=\sum_{u=1}^{Ne}\frac{c^{l+1}}{4\pi}\frac{2l+1}{(l(l+1))^n}\frac{(l-m)!}{(l+m)!}(2-\delta_{m0})X(u)P_l^m(\cos\theta_u)\cos m\varphi_u$$

$$H_l^m(3)=\sum_{u=1}^{Ne}\frac{c^{l+1}}{4\pi}\frac{2l+1}{(l(l+1))^n}\frac{(l-m)!}{(l+m)!}(2-\delta_{m0})X(u)P_l^m(\cos\theta_u)\sin m\varphi_u$$

$$G_0^0(3)=d;\ H_0^0(3)=0 \tag{27}$$

By utilizing the spatial filter $K_l(3)$ that connects the SHS of the scalp potential with the ME of the brain electrical generator (Eq. (5)), we get the ME: g_l^m, h_l^m and by utilizing the other spatial filters (Eqs. (5), (13), (16) and (19)), we get all the other SHS and respective imaging maps.

3.2. Inverse calculation and discussion

In the inverse calculation, the number of electrodes is 128 and they are distributed approximately uniformly on the upper hemisphere surface. The forward scalp potential is calculated according to Eq. (4) at $r=1.0$ and $Lmax=150$. The source model is the three dipoles as noted above. Ten percent Gaussian white noise is added to the scalp potential (the percentage noise level is defined by the ratio of the standard variance of the noise and that of the signal). Fig. 7 shows the forward SHS (Fig. 7a), and reconstructed SHS (Fig. 7b), and their difference (Fig. 7c). It is clear that though the maximum absolute error is at low spatial frequency, the maximum relative error is on the high frequency, and so it is unnecessary to include much higher frequency in the inverse calculation because a ill high frequency component provides nothing but misleading us. Based on our numeric tests, we believe that $Lmax=15$ (the number of the SHS terms is 255) is enough for inverse practice.

Fig. 8 shows the normalized SHS and maps of the reconstructed potentials in an infinite conductor model. The sources are imaged in a sense of a relative high resolution to the forward scalp potential maps (Fig. 5d,h) and a relative low resolution to the forward PCPM maps (Fig. 4), and the reason is clearly illustrated by the difference of the SHS shown on these figures. The map at $r=0.87$ (Fig. 8b) is previously called PCPM (Yao and Qi, 1995).

Fig. 9 shows the normalized SHS and maps of the recon-

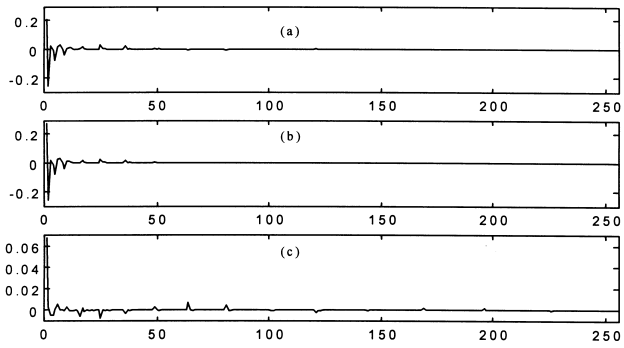

Fig. 7. The reconstructed SHS of the scalp potential. (a) The forward SHS of the scalp potential of the three dipoles in the concentric 3 sphere model, the horizontal axis is the order number of the SHS. It is ordered according to $G_1^0(3), G_1^1(3), H_1^1(3), G_2^0(3), G_2^1(3), H_2^1(3), ...G_{15}^{15}(3), H_{15}^{15}(3)$, and the total number is 255 for $Lmax = 15$; (b) the reconstructed SHS; (c) The difference between (a) and (b).

structed potentials in the concentric 3 sphere conductor, where Fig. 9b at $r = 0.87$ is the strict cortical surface potential map, the CPM, and it shows that the 3 sources could be imaged by the CPM.

Fig. 10 shows the normalized SHS and maps of the reconstructed ECM, EDM and LM. The sources are distinguished, too.

Based on these maps, all the five mappings provide higher spatial resolution than the conventional scalp potential map does (Fig. 5d,h). And so, each of them forms a high spatial resolution EEG mapping technique as the references emphasized. Comparing the forward (Figs. 4–6), and the inverse (Figs. 8–10), the difference is clear. And the reason is the limited precision of the SHS reconstruction especially on its high frequency component as shown by Fig. 7. The limited reconstruction precision of the SHS is due to the finite number of the electrodes on the scalp surface, the unavoidable measurement noise and the inverse algorithm with regularization smooth.

Fig. 11 shows the correlation coefficients (CC) versus various percentage noise levels (%). It shows that:

1. The CC order between the forward and inverse map of each of the five mappings is CPM > EDM > PCPM/LM > ECM as shown in Fig. 11a;
2. The LM has been thought to be approximately identical to the cortical potential (Nunez et al., 1994). Here, we suppose that the actual cortical potential map, the actual CPM, is the desired imaging map, the others are referenced to a 'surrogate' of the CPM, and then Fig. 11b shows that the reconstructed CPM is the best surrogate of the actual CPM, and the correlativity order is CPM ≥ EDM > PCPM > LM > ECM.

These results show that the CPM is the easiest one to be reconstructed by the inverse algorithm used in this paper.

3.3. Experimental comparisons of the five mappings

Fig. 12 shows an example of the five imaging techniques. The number of electrodes is 120, their positions are defined as the projection points on the corresponding best-fit sphere surface of group averaged electrode positions over 10 subjects (NeuroScan System). The potential data is group averaged VEP, too. And average reference is used in the algorithm. The noise/signal ratio is estimated by utilizing the recorded data before stimulation as the noise background, and the result is 14%.

Fig. 12 clearly shows that higher spatial resolution mappings of the electrical activities on the visual cortex are obtained, and the CPM, EDM and PCPM show a little higher signal/noise ratio than LM and ECM does.

4. Conclusion and discussion

In this paper, the five high-resolution EEG mappings are

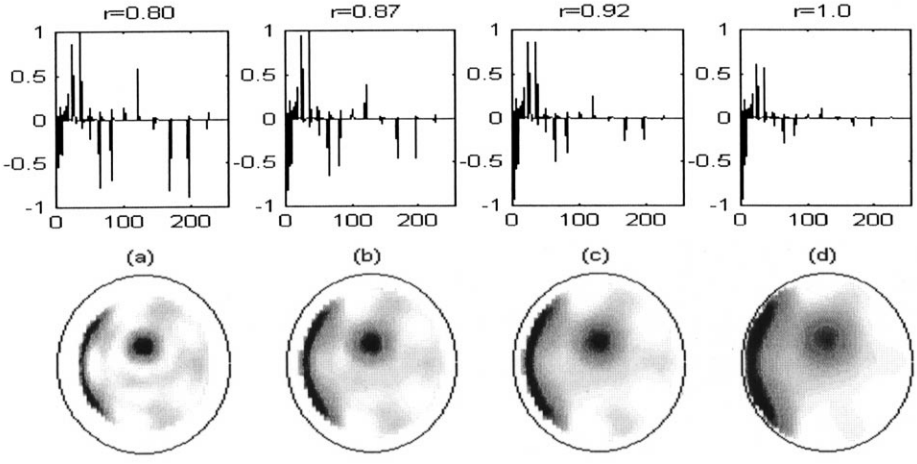

Fig. 8. The reconstructed SHS and maps of the potentials in the equivalent homogenized conductor model (Fig. 1b). The first row shows the normalized SHS at $r = 0.80$, 0.87, 0.92 and 1.0, respectively. Where the horizontal axis is the order number of the SHS. The second row shows the maps of the reconstructed potential at $r = 0.80$, 0.87, 0.92 and 1.0, respectively.

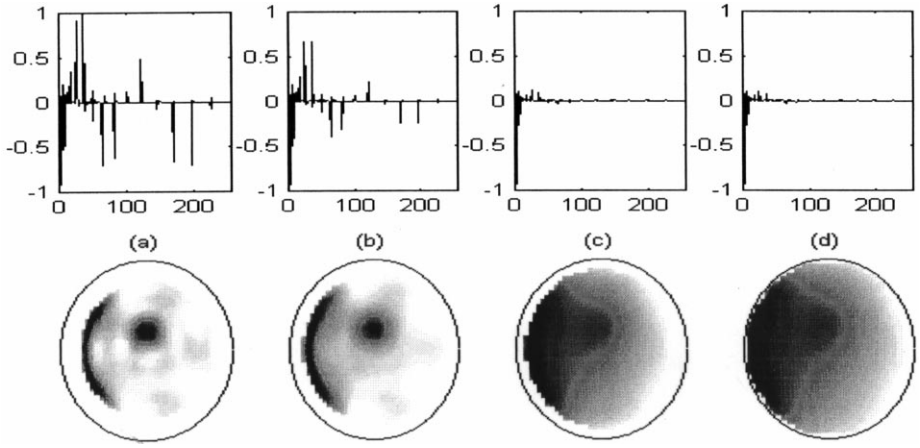

Fig. 9. The reconstructed SHS and maps of the potentials in the concentric 3 sphere conductor model. The first row shows the normalized SHS at $r = 0.80$, 0.87, 0.92 and 1.0, respectively. Where the horizontal axis is the order number of the SHS. The second row shows the maps of the reconstructed potential at $r = 0.80$, 0.87, 0.92 and 1.0, respectively.

unified in a frame of the SHS. And it is investigated that the theoretical relations with the ME of the actual electrical generator and relative imaging quality of these mappings. Based on the forward theoretical analyses, the ECM, LM and PCPM bring on higher resolution maps than the CPM does, and the EDM brings on an approximately equivalent resolution map to the CPM does. And so, if we could get a good reconstruction of the actual SHS, the ECM, LM and PCPM would be superior to the CPM and the EDM. However, due to many practical limitations in EEG measurement and reconstruction algorithm, the reliable high spatial frequency is limited in the reconstructed SHS. The inverse practice reported here shows that the CPM is the easiest one to be restored, and the second is the EDM. Due to the low-pass characteristics of the spatial filters of the EDM and CPM, they are less affected by the reconstructed low-precision high frequency components than the other three maps are. The high-resolution characteristics of the CPM and EDM, compared with the conventional scalp map, are mainly due to the interpolation from the scalp to the cortical surface.

As shown above, a precise SHS, and so a precise ME, will bring on a good reconstruction of all the five imaging maps. But it is impossible to reconstruct the SHS precisely in practice. So in order to get a good reconstruction of a specified map, a corresponding special algorithm is needed. For example, in order to suppress the noisy high spatial components in LM and ECM, a regularization algorithm with stronger smoothing effect on SHS is preferred. However, the improvement on signal/noise ratio of the imaging map by a smoother SHS of the LM and ECM will be accompanied by a decrease of the spatial resolution, thus resulting in a similar SHS and maps to that of the CPM, EDM or PCPM. Such a fact indicates that a relative priority order of the different mapping techniques stands only in a specified reconstruction and evaluation method, and different algo-

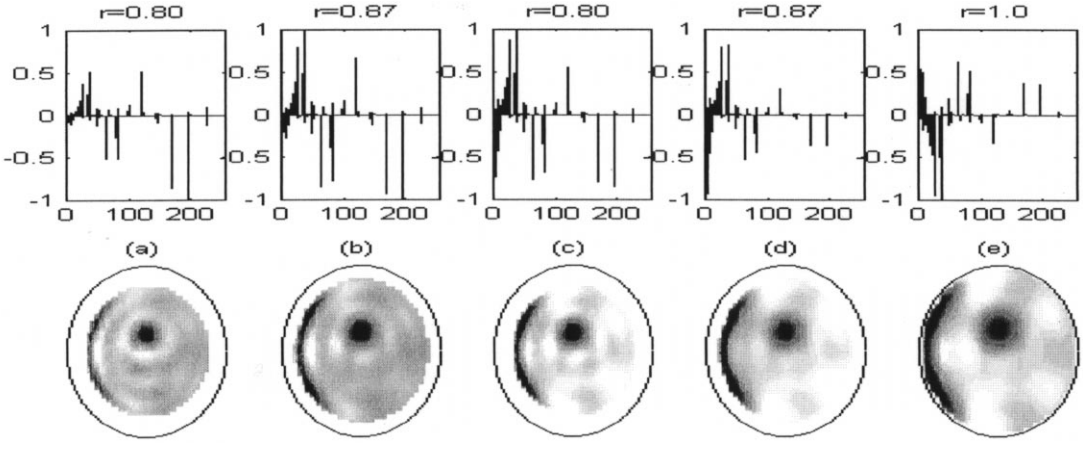

Fig. 10. The reconstructed SHS and maps of the ECM, EDM and LM. The first row shows the normalized SHS, and from left to right, they are successively the SHS of the ECM at $r = 0.80$ and 0.87, of the EDM at $r = 0.80$ and 0.87, and of the LM at $r = 1.0$. The second row shows the reconstructed ECM ((a) at $r = 0.80$ and (b) at $r = 0.87$), EDM ((c) at $r = 0.80$ and (d) at $r = 0.87$) and LM (e).

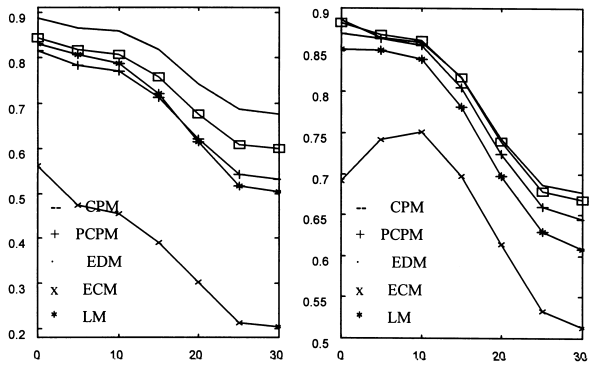

Fig. 11. Reconstruction comparison by correlation coefficient(CC). The horizontal axis is the various noise levels in percentage, and the vertical axis is the CC. The CCs between the forward CPM ($r = 0.87$), PCPM ($r = 0.87$), EDM ($r = 0.87$), ECM ($r = 0.87$), LM ($r = 1.0$) and the reconstructed CPM, PCPM, EDM, ECM, LM at the same corresponding depth, respectively; (b) The CCs between the forward CPM ($r = 0.87$) and the reconstructed CPM ($r = 0.87$), PCPM ($r = 0.87$), EDM ($r = 0.87$), ECM ($r = 0.87$) and LM ($r = 1.0$), respectively.

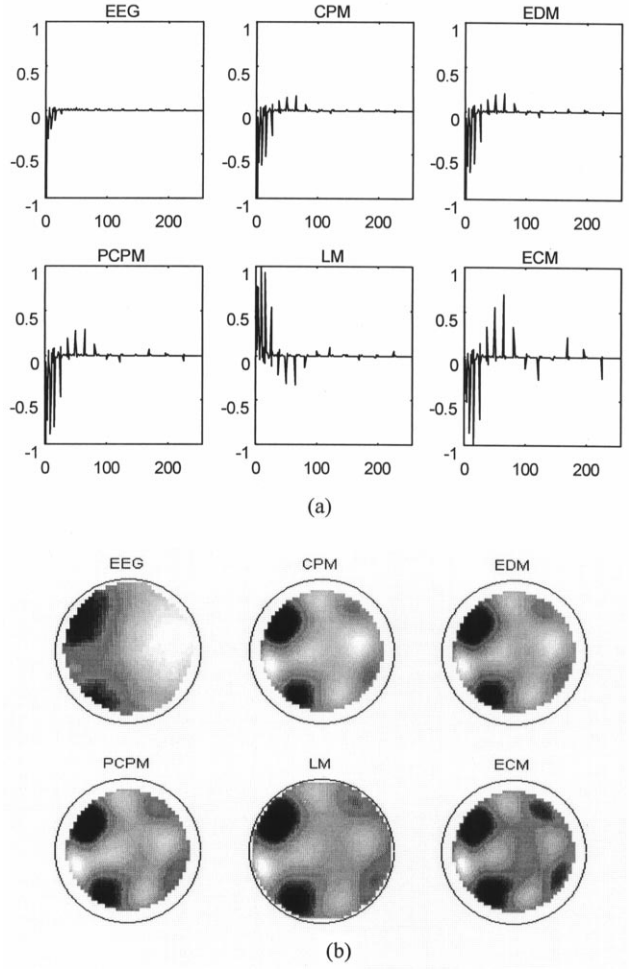

Fig. 12. The reconstructed SHS and maps of an empirical example. (a) The SHS of the scalp potential and the five maps, (b) scalp potential map and the 5 imaging maps. On the figure, EEG is the scalp potential map at 100 ms after a visual stimulation by a checkerboard flashed to the right visual field. CPM, EDM, PCPM and ECM are calculated at $r = 0.87$ and LM is at $r = 1.0$.

rithm may result in a different order. Therefore, the order given in this paper is a result of the algorithm used in this paper. The SHS theoretical frame reveals that there is a common basis of the five mappings, which is the ME of the actual electrical generator. The five maps are different filter outputs of the ME. And, in our opinion, the comparison and evaluation of the current techniques and future algorithms should be based on the quality of the reconstruction of the ME of the actual electrical generator. This viewpoint means that much more effort should be focussed on developing a better strategy to reconstruct the SHS of the scalp potential or to say the ME of the generator in the future.

According to the references (Oostendorp and Oosterom, 1996; Babiloni et al., 1996; Gevins et al., 1993; He et al., 1997; Van Burik et al., 1997), the LM, EDM and CPM have been implemented on a realistic head model. Moreover, some of those algorithms can be easily extended to implement PCPM and ECM on a realistic head model. The common basis, the SHS of potential in an infinite medium or to say the ME of the actual electrical generator, of the five mappings can be reconstructed not only when the head model is a spherical sphere model but also when it is a realistic layer-model. For example, an equivalently distributed dipole/charge layer may be reconstructed in a multilayer realistic head model by one of the reported algorithms (Babiloni et al., 1997; Zanow 1997). Then the multiple expansion of the obtained equivalent sources will bring on a reconstruction of the ME of the actual electrical generator. And then the five maps, and even more maps based on new designed filters in the future, may be deduced from the obtained SHS or ME.

Acknowledgements

The author wishes to thank the editor Prof. P.M. Rossini and other unknown referees for their constructive comments on this paper. This work is supported by a grant from the National Nature Science Foundation of China (No. 39770215), and a grant from the Huoyingdong Young Investigator Foundation of the Education Ministry of China.

References

Ahlfors SP, Ilmoniemi RJ, Hamalainen MS. Estimates of visually evoked cortical currents. Electroenceph clin Neurophysiol 1992;82:225–236.

Babiloni F, Babiloni C, Carducci F, Fattorini L, Onorati P, et al. Spline Laplacian estimate of EEG potentials over a realistic magnetic resonance-constructed scalp surface model. Electroenceph clin Neurophysiol 1996;98:363–373.

Babiloni F, Babiloni C, Carducci F, Fattorini L, Anello C, Onorati P, Urbano A. High resolution EEG: a new model-dependent spatial deblurring method using a realistically-shaped MR-constructed subject's head model. Electroenceph clin Neurophysiol 1997;102:69–80.

Baillet S, Garnero L. A Bayesian approach to introducing anatomo-func-

tional priors in the EEG/MEG inverse problem. IEEE Trans Biomed Eng 1997;44:374–385.
Biggins CA, Fein G, Raz J, et al. Artifactually high coherences result from using spherical spline computation of scalp current density. Electroenceph clin Neurophysiol 1991;79:413–419.
Edlinger G, Wach P, Pfurtscheller G. On the realization of an analytic high-resolution EEG. IEEE Trans Biomed Eng 1998;45:736–745.
Freeman W. Use of spatial de-convolution to compensate for distortion of EEG by volume conductor. IEEE Trans Biomed Eng 1980;37:421–429.
Gevins A. Dynamic functional topography of cognitive tasks. Brain Topogr 1989;2:37–56.
Gevins A. The future of electroencephalography in assessing neurocognitive functioning. Electroenceph clin Neurophysiol 1998;106:165–172.
Gevins A, Le J, Martin N, Reutterm B. High resolution EEG: 124-channel recording, spatial enhancement and MRI integration methods. Electroenceph clin Neurophysiol 1993;90:337–358.
Hamalainen, M., Ilmoniemi, R. Interpreting measured magnetic fields of the brain: estimates of current distributions, Report TKK-F- A559. Helsinki: University of Technology, 1984.
He B, Wang Y, Pak S, Ling Y. Cortical source imaging from scalp electroencephalograms. Med Biol Eng Comput 1996;34(Suppl. part 2):257–258.
He B, Wang Y, Wu D. Imaging brain electrical activity using a 3D realistically shaped inhomogeneous head model. Proc IEEE/EMBS 1997;1167–1169.
Hjorth B. An online transformation of EEG scalp potentials into orthogonal source derivations. Electroenceph clin Neurophysiol 1975;39:26–530.
Kearfott R, Sidman R, Major D, Hill C. Numerical tests of a method for simulating electrical potential on the cortical surface. IEEE Trans Biomed Eng 1991;38:294–299.
Kirsch, A. An introduction to the mathematical theory of inverse problems. New York: Springer, 1996.
Law SK, Nunez PL. High resolution EEG using spline generated surface Laplacians on spherical and ellipsoidal surfaces. IEEE Trans Biomed Eng 1993;40:145–153.
Le J, Gevins A. Method to reduce blur distortion from EEG's using a realistic head model. IEEE Trans Biomed Eng 1993;40:517–528.
Le J, Menon V, Gevins A. Local estimate of surface Laplacian derivation on a realistically shaped scalp surface and its performance on noisy data. Electroenceph clin Neurophysiol 1992;92:433–441.
Manahilov V, Riemslag FC, Spekreijse H. The Laplacian analysis of the pattern onset response in man. Electroenceph clin Neurophysiol 1992;82:220–224.
Nunez PL. Electric fields of the brain: the neurophysics of EEG. New York: Oxford University Press 1981. pp. 196–203.
Nunez PL. Removal of reference electrode and volume conduction effects by spatial deconvolution of evoked potentials using a three-concentric sphere model of the head. Electroenceph clin Neurophysiol 1987;(Suppl. 39):143–148.
Nunez PL. Estimation of large scale neocortical source activity with EEG surface Laplacians. Brain Topogr 1989;2:141–154.
Nunez PL, Silibertein RB, Cdush PJ, Wijesinghe RS, Westdrop AF, Srinivasan R. A theoretical and experimental study of high resolution EEG based on surface Laplacian and cortical imaging. Electroenceph clin Neurophysiol 1994;90:40–57.
Oostendorp TF, Oosterom AV. The surface Laplacian of the potential: theory and application. IEEE Trans Biomed Eng 1996;43:394–405.
Pascual-Marqui RD, et al. Current source density estimation and interpolation based on the spherical harmonic Fourier expansion. Int J Neurosci 1988;43:237–249.
Perrin F, Pernier J, Bertrand O, et al. Mapping of scalp potentials by surface spline interpolation. Electroenceph clin Neurophysiol 1987;66:75–81.
Perrin F, Pernier J, Bertrand O, Echallier JF. Spherical splines from scalp potential and current density mapping. Electroenceph clin Neurophysiol 1989;72:184–187.
Rush S, Driscoll DA. Current distribution in the brain from surface electrodes. Anesth Analg 1968;47:717–723.
Rush S, Driscoll DA. EEG electrode sensitivity – an application of reciprocity. IEEE Trans Biomed Eng 1969;16:15–22.
Sidman R, Ford M, Ramsey G, Schlichting C. Age-related features of the resting and P300 auditory evoked responses using the dipole localization method and cortical imaging technique. J Neurosci Methods 1990;33:22–32.
Sidman R, Vincent D, Smith D, Lee L. Experimental tests of the cortical imaging technique-applications to the response to median nerve stimulation and the localization of epileptiform discharges. IEEE Trans Biomed Eng 1992;39:437–444.
Srebro R. An iterative approach to the solution of the inverse problem. Electroenceph clin Neurophysiol 1996;98:349–362.
Srebro R, Oguz RM. Estimating cortical activity from VEPs with the shrinking ellipsoid inverse. Electroenceph clin Neurophysiol 1997;102:343–355.
Srebro R, Oguz RM, Hughlett K, Purdy PD. Estimating regional brain activity from evoked potential field on the scalp. IEEE Trans Biomed Eng 1993;40:509–516.
Srinivasan R, Nunez PL, Tucker DM, et al. Spatial sampling and filtering of EEG with spline Laplacians to estimate cortical potentials. Brain Topogr 1996;8:355–367.
Stratton, J.A. Electromagnetic Theory, New York: McGraw-Hill, 1941.
Towle VL, Cohen S, Alperin N, et al. Displaying electrocorticographic findings on gyral anatomy. Electroenceph clin Neurophysiol 1995;94:221–228.
Van Burik M, Edlinger G, Peters M, Pfurtscheller G. Calculating cortical potentials using the boundary element method. Biomedizinische Technik, Band 42, Erganzungsband 1997;1:185–188.
Wahba G. Spline interpolation and smoothing on the sphere. Siam J Sci Stat Comput 1981;2:5–16.
Wang JZ, Williamson SJ, Kaufman L. Magnetic source images determined by a least-field analysis: the unique minimum-norm least-squares estimation. IEEE Trans Biomed Eng 1992;39:665–675.
Wang Y, He B. A computer simulation study of cortical imaging from scalp potentials. IEEE Trans Biomed Eng 1998;45:724–735.
Yao D. Equivalent source method and three-dimension EEG imaging. J Biomed Eng 1995a,12(4):322-341 (in Chinese).
Yao D. Basic theory of the equivalent distributed source cortical imaging technique. Proc Chinese Biomed Eng Soc 1995b;October:193-194 (in Chinese).
Yao D. Imaging of EEG by spherical harmonic analysis. J Electron 1995c;17:456-462 (in Chinese).
Yao D. The equivalent source technique and cortical imaging. Electroenceph clin Neurophysiol 1996a;98:478–483.
Yao D. Theory and simulation of the cortical imaging techniques by spherical harmonic analysis. J Univ Electronic Sci Technol China 1996b;25(8):224-229 (in Chinese).
Yao D, Luo B. Theory of the EEG cortical imaging techniques. Chinese J Biomed Eng 1996a;5(3):128-136 (English edition).
Yao D, Luo B. A new algorithm for the three-dimensional imaging of EEG and its simulation results. Chinese J Biomed Eng 1996b;15:295-300 (in Chinese).
Yao D, Qi J. A new algorithm for the cortical imaging. J Univ Electronic Sci Technol China 1995;24(2):175-180 (in Chinese).
Zanow F. Realistically shaped models of the head and their applications to EEG and MEG. Ph.D. Thesis, Twente: University of Twente, 1997.
Zhao F, Wu D, et al. A new realistic geometry spline Laplacian algorithm and its application to VEP. 20th IEEE /EMBS, Hong Kong, October, 1998.